Effect of Rainfall Transients on Thermal and Moisture Exposure of Underground Electric Cables

Jeffrey S. Marshall and Andrew P. Fuhrmann
School of Engineering, The University of Vermont

Corresponding Author: Jeffrey S. Marshall, School of Engineering, The University of Vermont, Burlington, VT 05405, U.S.A. PHONE: 1 (802) 656-3826,
EMAIL: jmarsha1@uvm.edu.

Keywords: underground cables; cable heat transfer; moisture transport; thermal engineering; power cable insulation; rainfall

Abstract

Cable ampacity analysis is generally performed assuming constant worst-state environmental conditions, which often correspond to a dry soil condition or to a condition with uniform ambient soil moisture content. The characteristic time scale of thermal variation in the soil is large, on the order of several weeks, and is similar to the time scale between rainfall events in many geographic locations. Intermittent rainfall events introduce significant transient fluctuations that influence the thermal conditions and moisture content around a buried cable both by increasing thermal conductivity of the soil and by increasing the moisture exposure of the cable insulation. This paper reports on a computational study of the effect of rainfall events on the thermal and moisture transients surrounding a buried cable. The computations were performed with a finite-difference method using an overset grid approach, with an inner polar grid surrounding the cable and an outer Cartesian grid. The thermal and moisture transients observed in computations with periodic rainfall events were compared to control computations with a steady uniform rainfall. Under periodic rainfall conditions, the temperature and moisture fields are observed to approach a limit-cycle condition in which the cable surface temperature and moisture content oscillate in time, but with mean values that are significantly different than the steady-state values.

Nomenclature

Roman letters

A_g = area of outer grid cell [m^2]

b = cable submergence depth [m]

c_S = specific heat of soil [$J/kg \cdot K$]

c_w = specific heat of liquid water [$J/kg \cdot K$]

C = effective soil heat capacity [$J/m^3 \cdot K$]

C_w = heat capacity of water [$J/m^3 \cdot K$]

d = cable diameter [m]

D = rainfall duration parameter ($= \tau_R / \tau_L$) [dimensionless]

D_{TL} = liquid thermal migration coefficient $\left[m^2/s \cdot K\right]$

D_{TV} = vapor thermal migration coefficient $\left[m^2/s \cdot K\right]$

D_T = total thermal migration coefficient $\left[m^2/s \cdot K\right]$

$D_{\theta L}$ = liquid isothermal diffusivity $\left[m^2/s\right]$

$D_{\theta V}$ = vapor isothermal diffusivity $\left[m^2/s\right]$

D_θ = total isothermal diffusivity $\left[m^2/s\right]$

F = dimensionless rainfall period ($= \tau_P / \tau_L$) [dimensionless]

f_{out} = heat supply rate to each outer grid cell [W/m^3]

h = convective heat transfer coefficient [W/m^2K]

h_{lv} = specific enthalpy of vaporization [J/kg]

H_x, H_y = grid size in x and y-directions [m[

I = rainfall intensity parameter ($= \overline{Q}_{rain} / K_{\theta 0}$) [dimensionless]

K_e = Kersten number [dimensionless]

K_θ = hydraulic conductivity [m/s]

L = latent heat of vaporization [J/m^3]

N_c = number of outer grid cells which receive a heat supply [dimensionless]

q_{surf} = cable heat flux per unit depth [W/m^2]

$\overline{q}$ = average cable surface heat flux [W/m^2]

Q = net water flux [m/s]

Q_{rain} = liquid flux due to rainfall, per unit depth [m/s]

r = radial coordinate [m]

R = cable radius ($= d/2$) [m]

R_I = radius of inner grid [m]

S = effective saturation ($= \theta / \theta_{sat}$) [dimensionless]

t = time [s]

T = absolute temperature [K]

T_f = temperature value at fringe point [K]

T_0 = ambient temperature [K]

T_{surf} = average temperature around cable surface [K]

x = horizontal coordinate [m]

y = vertical coordinate [m]

$v_{\max}$ = maximum liquid velocity magnitude [m/s]

$\mathbf{v}$ = liquid velocity [m/s]

Greek letters

ϕ = azimuthal coordinate [dimensionless]

η = soil porosity [dimensionless]

λ = effective thermal conductivity of soil $[\mathrm{W/m \cdot K}]$

λ_{dry} = thermal conductivity of dry soil $[\mathrm{W/m \cdot K}]$

λ_{sat} = thermal conductivity of saturated soil $[\mathrm{W/m \cdot K}]$

θ = moisture content [dimensionless]

θ_f = value of moisture content at fringe point [dimensionless]

θ_{sat} = moisture content of saturated soil ($= \eta$) [dimensionless]

θ_{surf} = average moisture content around cable surface [dimensionless]

ρ_s = effective density of soil [$\mathrm{kg/m^3}$]

ρ_w = density of liquid water [$\mathrm{kg/m^3}$]

τ = time scale [s]

τ_C = convective time scale ($= b / K_{\theta 0}$) [s]

τ_D = diffusive time scale ($= C_0 b^2 / \lambda_0$) [s]

τ_L = time scale of daily load variation [s]

τ_R = rain duration time scale [s]

τ_P = time scale between rain events [s]

ξ = dimensionless depth ($= -y / b$) [dimensionless]

1. Introduction

Determination of the current-carrying capacity (or ampacity) of underground electric cables is one of the key factors limiting operation of electric distribution systems, particularly in residential areas. Cable lifespan depends in a nonlinear manner on several factors, primary among which are insulation temperature, electric stress magnitude, and exposure of insulation to moisture (Hyvönen, 2008). The effect of temperature on insulation lifespan is often approximated by an exponential (Arrhenius) expression (Montanari et al., 2002; Mazzanti, 2007, 2009), so that the peak temperature values have a disproportionately large influence on lifespan degradation compared to the average temperature value. In order to reduce peak temperatures, ampacity is usually set for cable systems based on worst-case environmental conditions, usually consisting of dry conditions or conditions with uniform background soil moisture content. Water has a duel role on the cable lifespan. On the one hand, the thermal conductivity of soil is substantially increased by the presence of water, with an increase of an order of magnitude or more between dry and saturated conditions for many soils (Hamdhan and Clarke, 2010). As a consequence, the presence of water decreases insulation temperatures, which has a favorable effect on cable lifespan. On the other hand, exposure to water can give rise to formation of water treeing degradation within the cable insulation (Hyvönen, 2008), which over time can lead to deterioration of the insulation material and shortening of the cable lifespan.

The increasing availability of plug-in electric vehicles (PEVs) is expected to substantially increase electric loads in the near future, particularly within residential communities where underground cable systems are commonly used (Fernández et al.,

2011; Webster, 1999; Clement-Nyns et al., 2010). Moreover, the electric load associated with PEVs has large stochastic variation, depending on the percentage of a community that has electric vehicles. In order to accommodate residential PEVs while minimizing the cost of upgrading infrastructure, new charge-control schemes have been proposed to better manage electricity availability in distribution systems without exceeding load limits (Rezaei et al., 2014).

In the presence of large fluctuations of the electric load, it is important to have a good understanding of other transients imposed on the heat and moisture transfer around the cable, the most important of which originate from intermittent rainfall events. Rainfall is a key factor in determination of cable temperature and water exposure under actual environmental conditions. In many geographic areas around the world, between 25-40 rainy days during a year account for two-thirds of the total annual precipitation (Sun et al., 2006). This range corresponds to a typical average interval of 9-14 days between significant rainfall events. The range of time intervals associated with rainfall events is therefore similar to the time scale associated with heat transfer in the soil surrounding an underground cable (Anders, 1997), with the consequence that the temperature field around underground cables in regions with frequent rainfall may be nearly always in a transient state, influenced on a short time scale by the daily load variation and on a longer time scale by soil moisture variation associated with rainfall.

There is a substantial literature on prediction of cable ampacity based on thermal analysis within cables and the soil surrounding the cables. A survey of steady-state analytical methods is given by Neher and McGrath (1957), which has also been extended to transient problems (Neher, 1964; Anders and El-Kady, 1992; Liang, 1999; Black and

Park, 1983). These analytical models are subject to a number of simplifications, including the assumption that the ground surface is an isotherm, that cables are a line source of heat, and for transient calculations, that the heat source changes as a series of discrete step functions. Numerical solutions for cable thermal fields have been reported using the finite-element method (Flatbo, 1973; Kellow, 1981; Nahman and Tanaskovic, 2012), the finite-volume method (Freitas et al., 1996), and a boundary-element method (Gela and Dai, 1988). Application of overset grid methods to cable thermal analysis were reported by Garrido et al. (2003), Vollaro et al. (2011), and Marshall et al. (2013). Overset grid methods are well suited for cable heat transfer problems since the characteristic length scale for heat transfer varies over a large range, from the cable diameter to the submergence depth of the cable. Problems with soil heterogeneity on cable heat transfer were examined by Tarasiewicz et al. (1985) and Hanna et al. (1993), and nonlinear effects due to temperature-dependent insulation electrical resistance was examined by Kovač et al. (2006).

The effect of moisture variation on underground cable thermal fields was first examined computationally by Anders and Radhakrishna (1988) using a finite element method, and later by Freitas et al. (1996) using a finite volume method. Both of these studies neglect thermal convection caused by fluid velocity associated with moisture gradients, and they assume that the ambient moisture level is uniform. Specifically, the studies assume that no additional moisture is added to the system at the soil-air interface (i.e., no rainfall). A primary observation of these studies is the formation of a local dry region surrounding an underground cable, within which the temperature gradient associated with the cable thermal field causes moisture to migrate away from the cable.

The presence of this dry region decreases the soil thermal diffusivity in the region surrounding the cable, which in turn increases the cable surface temperature. Moya et al. (1999) report an experimental study of heat and moisture transport around a heated cylinder in unsaturated soil. The experimental results are found to compare well with numerical computations using a finite-volume method. The paper concluded that the primary influence of moisture on the cable surface temperature is through the influence of moisture on the soil thermal conductivity. This observation might seem to justify the common approach of simply prescribing a conservative thermal conductivity value for the soil and determining ampacity using only solution of the thermal equation. However, one problem with that approach is that cable insulation degradation is sensitive not only to thermal conditions, but also to water exposure. Accurate calculation of cable moisture exposure in realistic weather conditions is critical in order to adequately characterize degradation associated with these two variables.

The current paper examines the effect of transients caused by rainfall events on the temperature and moisture fields surrounding an underground cable. Of particular interest is the effect of a rainfall front on the dry region surrounding the cable, and the transients caused by passage of rain fronts at different rainfall intensities, durations, and frequencies. A two-dimensional finite-difference model is used to simulate both the temperature and moisture fields surrounding an underground cable. The top boundary condition for the moisture field at the soil-atmosphere interface is varied to represent effect of rainfall of different intensity, duration, and frequency. Unlike most studies of combined moisture/thermal cable analysis, we retain the thermal convection term in the temperature governing equation to account for the short time scales of the rain front. The

significance of the thermal convection term is examined by comparing simulations both with and without this term.

A summary of the governing equations and boundary conditions, and of the computations method used to solve thee equations, is given in Section 2. This section also includes results of a grid independence study and an evaluation of the importance of thermal convection on the cable surface temperature. The results of the paper are presented in Section 3, including comparison of steady-state calculations with constant rainfall rate with periodic rainfall cases having rainfall events with different intensity, duration, and frequency. Conclusions are given in Section 4.

2. Computational Method

Governing Equations

The governing equations for heat and moisture transfer within the ground are given by the coupled system derived by Philip and de Vries (1957) as

$$C\frac{\partial T}{\partial t} + C_w \mathbf{v}\cdot\nabla T = \nabla\cdot(\lambda\nabla T) + \nabla\cdot(L\,D_{\theta V}\nabla\theta), \tag{1}$$

$$\frac{\partial \theta}{\partial t} = \nabla\cdot(D_T\nabla T) + \nabla\cdot(D_\theta\nabla\theta) + \frac{\partial K_\theta}{\partial y}, \tag{2}$$

where $T(\mathbf{x},t)$ is the temperature field and $\theta(\mathbf{x},t)$ is the volumetric moisture content. The various coefficients in (1)-(2) include the volumetric heat capacity of wet soil *C*, the volumetric heat capacity of water C_w, the water velocity vector $\mathbf{v}$, the unsaturated hydraulic conductivity K_θ, the soil thermal conductivity λ, the latent heat of

vaporization of water L, the thermal moisture diffusivity D_T, the isothermal moisture diffusivity D_θ, and the isothermal vapor diffusivity $D_{\theta V}$. Equation (1) is derived from the conservation of energy, where the second term on the left-hand side represents thermal convection by the liquid motion, and on the right-hand side, the first term represents thermal diffusion, and the second term represents energy transfer via latent heat of the vapor caused by a moisture gradient.

Equation (2) is derived from a combination of the continuity equation and an extension of Darcy's law to unsaturated media. The continuity equation gives an expression for the rate of change of the moisture content as

$$\frac{\partial \theta}{\partial t} + \nabla \cdot \mathbf{Q} = 0, \tag{3}$$

where $\mathbf{Q}$ is the net water flux (defined to be positive upward), which is equal to the product of the water velocity $\mathbf{v}$ and the soil porosity η. An equation for $\mathbf{Q}$ was derived by Philip and de Vries (1957) in terms of the temperature and moisture gradients as

$$\mathbf{Q} = \mathbf{v}/\eta = -(D_T \nabla T + D_\theta \nabla \theta + K_\theta \mathbf{e}_y), \tag{4}$$

where the first and second terms on the right-hand side are associated with transport of water by capillary action and the third term is associated with gravitational transport. Substituting this expression into the continuity equation (3) gives the moisture balance equation (2). Equations (1)-(2) are the same equations used by previous investigators for

cable ampacity computation (Anders and Radhakrishna, 1988; Freitas et al., 1996; Moya et al., 1999), with the difference that we have also included the thermal convection term in order to properly account for the effect of rainfall on the temperature field.

The coefficients λ, D_T, D_θ, L, C, $D_{\theta V}$, and K_θ are functions of the temperature and moisture content. Since analytical expressions for these coefficients are difficult to obtain, it is common practice to evaluate them using empirical formulas developed for specific soil types. In the current study, a representative backfill soil was selected, which is identified as Soil III by Anders and Radhakrishna (1988). This soil is described as well-graded with course to fine particles, such as is found in a silty sand or a sandy loam. The equations used for the coefficients for this soil type are given by Anders and Radhakrishna (1988) as

$$\begin{aligned} &\lambda = (\lambda_{sat} + \lambda_{dry})K_e + \lambda_{dry}, \\ &D_T = D_{TL} + D_{TV}, \qquad D_\theta = D_{\theta L} + D_{\theta V}, \\ &L = \rho_w h_{lv}, \qquad C = \rho_s c_S + \rho_w c_w \theta \end{aligned} \tag{5}$$

where $K_e = \log S + 1$, $S \equiv \theta / \theta_{sat}$, and the various coefficients in (5) are given in Table 1. The empirical equation for effective thermal conductivity in (5) is restricted to $S \geq 0.1$. When $S < 0.1$, the soil is nearly dry, so we set $\lambda = \lambda_{dry}$ in the computations.

Table 1. Expressions used for the variable coefficients that characterize heat and moisture transport in the soil as functions of temperature T (in degrees Kelvin) and relative moisture content $S \equiv \theta / \theta_{sat}$. The different coefficients are in SI units, as indicated in the nomenclature section.

Variable Parameters		Constant Parameters
$D_{TL} = \exp(8.01S - 26.96)$		$\theta_{sat} = 0.45$
$D_{TV} = \exp(-1.416S - 23.316)$		$\lambda_{dry} = 0.3$
$D_{\theta L} = \exp(8.06S - 18.19)$		$\lambda_{sat} = 1.6$
$D_{\theta V} = \exp(-7.483S - 27.792)$		$\rho_s = 1800$
$h_{lv} = 2.496 \times 10^{-6} - (0.00237)T$		$\rho_w = 1000$
$K_\theta = 10^{-6} S^6$		$c_S = 1480$
		$c_w = 4216$

Computational Approach

The numerical computations are performed on both an outer Cartesian grid and on an inner polar grid surrounding a single buried cable, as shown in Figure 1. The outer grid has boundaries at $x = \pm \frac{1}{2} H_x$ in the horizontal direction, and it extends from the ground to a depth $y = -H_y$. The four boundaries of the outer grid are identified by circled numbers [1] - [4] in Figure 1. On the bottom boundary [4], the temperature is set to a prescribed value T_0 and the moisture content is governed by a flux balance of the form

$$D_T \frac{\partial T}{\partial y} + D_\theta \frac{\partial \theta}{\partial y} = -K_\theta . \qquad (6)$$

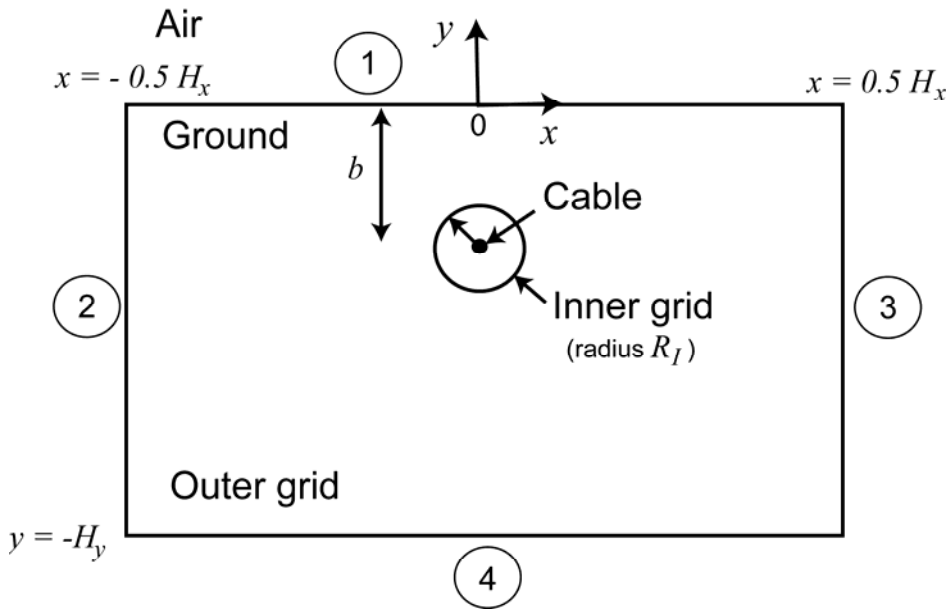

Figure 1. Schematic diagram of the computational flow domain and the inner (polar) and outer (Cartesian) grids, where the cable is identified as a black circle at the center of the inner grid, which is submerged a depth *b* below the ground. The boundaries of the outer grid are identified by circled numbers.

Zero-flux boundary conditions are used for temperature on the side boundaries [2] and [3], so that $\partial T / \partial x = 0$. The side boundary condition for moisture is again based on the flux balance, and is given by

$$D_T \frac{\partial T}{\partial x} + D_\theta \frac{\partial \theta}{\partial x} = 0 . \qquad (7)$$

A convective boundary condition for temperature is used on the top boundary [1], which has the form

$$\lambda \frac{\partial T}{\partial y} + h(T - T_{atm}) + LD_{\theta V} \frac{\partial \theta}{\partial y} = 0 \ , \tag{8}$$

where h is the surface heat transfer coefficient and T_{atm} is the atmospheric temperature. The third term is included along with the tradition convective boundary equation to account for the transfer of latent heat by vapor migration. The boundary condition for moisture content on the top boundary [1] is

$$D_T \frac{\partial T}{\partial y} + D_\theta \frac{\partial \theta}{\partial y} + K_\theta = Q_{rain} \, , \tag{9}$$

where $Q_{rain}(t)$ denotes the prescribed time-varying flux of water supply by rain on the top boundary.

The outer Cartesian grid computations are performed by introducing a heat source for grid cells of the outer grid that overlap the cable cross-section. The heat supply rate to each outer grid cell, f_{out}, is related to the cable surface heat flux q_{in} by

$$2\pi R q_{in} = N_c A_g f_{out} \, , \tag{10}$$

where R is the cable radius, N_c is the number of outer grid cells which receive a heat supply, and A_g is the area of one cell of the outer grid.

The outer grid yields an accurate solution for heat and moisture transport in the region sufficiently far away from the cable, but it does not satisfy the boundary

conditions on the cable surface. In order to obtain a more accurate solution near the cable, we use an overset inner grid in an annular region spanning from the cable radius R to the outer radius R_I of the inner grid. The center of the inner grid is located a distance b below the ground level, where b is called the cable burial depth. Within this inner grid, the temperature and moisture content fields are discretized using a polar coordinate system (r, ϕ). The inner grid solution satisfies the flux boundary condition in temperature and the no-penetration condition for moisture on the cable surface, so that

$$-\lambda \frac{\partial T}{\partial r} = q_{in}, \qquad \frac{\partial \theta}{\partial r} = 0 \qquad \text{on } r = R. \tag{11}$$

The two grids communicate on the set of grid points on the outer boundary of the inner grid ($r = R_I$), which are called *fringe points*. At each time step, we first solve for the temperature and moisture fields on the outer grid, and then use a bilinear interpolation to set the values of T and θ at the fringe points of the inner grid, denoted by T_f and θ_f. The inner solution is then solved using a Dirichlet boundary condition on its outer surface of the form

$$T = T_f, \qquad \theta = \theta_f \qquad \text{on } r = R_I. \tag{12}$$

The governing equations (1)-(2) for temperature and moisture content were solved within both the inner and outer grids using a Crank-Nicholson method for the diffusive terms and a second-order Adams-Bashforth method for the convective term, with the

velocity given by (4). Spatial derivatives were computed using second-order centered differences in both grids. The resulting system of equations was solved using a Gauss-Seidel iteration method, which was written such that computations are performed only with non-zero matrix elements. It is noted that (1) approaches a first-order hyperbolic equation in the absence of the diffusive terms, for which the numerical method described above would not be stable. This numerical instability was not an issue in the current computations, however, since the scale of the problem is fairly small (ranging from centimeters to tens of meters) and the diffusive terms were consequently sufficiently large to suppress the instability. The CFL number $v_{\max}\Delta t/\Delta x$ was monitored for all computations and did not exceed 0.002.

Dimensionless Parameters

The problem depends upon two dominant length scales - the cable diameter *d* and the cable submergence depth *b*. The cable diameter characterizes small-scale fluctuations of temperature and moisture around the cable, such as are associated with power load fluctuations during a daily cycle, but the submergence depth is more characteristic of the thermal and moisture fields as a whole.

Three characteristic time scales in the problem are referred to as the convective time scale τ_C, the diffusive time scale τ_D, and the load-variation time scale τ_L. If we select *b* as a characteristic length scale, the *convective time* $\tau_C = b/K_{\theta 0}$ is the typical time required for a rain front to propagate from the ground to the cable location, where $K_{\theta 0}$ is characteristic of the velocity scale caused by gravitational drainage. The *diffusive time* $\tau_D = C_0 b^2/\lambda_0$, where λ_0/C_0 is a characteristic thermal diffusivity, is representative

of the time required for the thermal field to attain a steady state upon change of the cable heat flux or of the surrounding moisture field. The *load-variation time* τ_L represents the period of oscillation of the cable heat load, where we make the common assumption that the cable load is periodic on a daily cycle. For typical conditions, τ_C is on the order of 11 days, τ_D is on the order of 20 days, and τ_L is 1 day. The addition of rain at the top boundary introduces other time scales which can be compared to the three time scales described above. These additional scales include the rain duration time τ_R and the period between rain events τ_P, both of which are examined in the paper.

A set of dimensionless variables are defined using the cable submergence depth *b* as a length scale, the load-variation time τ_L as the time scale, the average cable surface heat flux $\overline{q}$, and the ambient temperature T_0. The resulting dimensionless variables (denoted with primes) are defined by

$$T' = \frac{\lambda_0}{\overline{q} b}(T - T_0), \qquad \nabla' = b\nabla, \qquad dt' = dt/\tau_L, \quad x' = x/b, \qquad y' = y/b,$$

$$\mathbf{v}' = \mathbf{v}/K_{\theta 0}, \qquad f'_{out} = \frac{b}{\overline{q}} f_{out}, \qquad q'_{in} = q_{in}/\overline{q}, \qquad Q'_{rain} = Q_{rain}/K_{\theta 0},$$

$$C' = C/C_0 \qquad \lambda' = \lambda/\lambda_0 \qquad L' = L/L_0 \qquad D'_V = D_V/D_{V0},$$

$$D'_T = D_T/D_{T0}, \qquad D'_\theta = D_\theta/D_{\theta 0}, \qquad K'_\theta = K_\theta/K_{\theta 0}. \tag{13}$$

A subscript "0" is used to denote constant nominal values of the coefficients, where these nominal values are set equal to the coefficient values under saturated soil conditions (obtained from (5) and Table 1 with $S = 1$).

The dimensionless governing equations and boundary conditions contain a number of different dimensionless parameters. In the current paper, we hold many of these dimensionless parameters constant in order to focus on a small number of parameters that characterize the rainfall. Characteristic values of these dimensionless parameters are obtained for a typical 5kV distribution cable (e.g., a tape-shielded 5kV 4/0 AWG aluminum conductor), for which the average cable diameter is $d = 2.5\,\text{cm}$, the burial depth is $b = 1\,\text{m}$, and a typical cable surface heat flux is $\overline{q}$ = 500 W/m^2 for an average-size residential community (Marshall et al., 2013). Using a typical value for thermal conductivity of fully saturated soil of $\lambda_0 = 1.6\,\text{W/mK}$, we obtain a relationship between a change in the dimensionless temperature $\Delta T'$ and the dimensional temperature ΔT as $\Delta T = (312.5°C)\Delta T'$. A list of constant dimensionless parameters and the values used for these parameters in the current computations is given in Table 2. The dimensionless parameters that are allowed to vary in the computations include the rainfall intensity, the rainfall duration parameter $D_{rain} = \tau_R / \tau_L$, and the dimensionless rainfall frequency $f' = f\tau_L$.

Grid Independence and Validation

A grid independence study was performed to examine sensitivity of the computations to number of grid points in the inner and outer grids. Since the focus of the study is on effect of soil characteristics and rain on the thermal and moisture exposure of a buried cable, the grid independence study examines the effect of grid resolution on the average temperature and moisture content on the cable surface as a function of time. The

Table 2. List of dimensionless parameters whose values are held fixed, and their values in the current computations.

Parameter Name	Equation	Typical Value
H_{conv}	$\frac{hb}{\lambda_0}$	2.8
c_1	$\frac{\tau_L \lambda_0}{C_0 b^2}$	5.2×10^{-2}
c_2	$c_1 c_7$	1.2×10^{-10}
c_3	$\frac{\tau_L \bar{q} D_{T0}}{\lambda_0 b}$	0.16
c_4	$\frac{\tau_L D_{\theta 0}}{b^2}$	3.5
c_5	$\frac{\tau_L K_{\theta 0}}{b}$	8.6×10^{-2}
c_6	$c_5 \frac{\rho_w c_w}{C_0}$	0.14
c_7	$\frac{L_0 D_{V0}}{\bar{q} b}$	2.4×10^{-9}
c_8	$\frac{\lambda_0 D_{\theta 0}}{D_{T0} \bar{q} b}$	22
m_1	$\frac{\bar{q} D_{T0}}{\lambda_0 K_{\theta 0}}$	1.9
m_2	$\frac{D_{\theta 0}}{K_{\theta 0} b}$	40

test computation used for the grid independence study was conducted for a case where the initial temperature field is set equal to the ambient temperature ($T'(x,0)=0$) and the initial moisture content was $\theta(x,y)=0.1$. The domain size was $H_x/b=5.0$ and $H_y/b=3.0$, with a cable diameter $d/b=0.0249$ and an inner grid radius $R_I/b=0.0747$. The cable surface heat flux was held constant ($q'_{surf}=1$) and the rain flux was set at

$Q'_{rain} = 0.5$. The time step was fixed as $\Delta t' = 0.002$, and the runs were continued out to $t' = 20$. The number of grid points in the inner grid was set such that the grid spacing at the outer edge of the inner grid in both the radial and azimuthal directions was similar to the grid spacing used in the outer grid. In the grid independence study, the number of points in the inner and outer grids were varied in the same proportion. Three different grids were examined in the study, with grid point numbers in each direction in the inner and outer grids listed in Table 3. Results for the average cable surface temperature and moisture content are plotted in Figure 2 as functions of time for each grid. For the finest two meshes, the maximum difference in cable surface temperature was 0.5% and the maximum difference in moisture content was 1.1%. The computations in the remainder of the paper were performed on the medium-resolution mesh B.

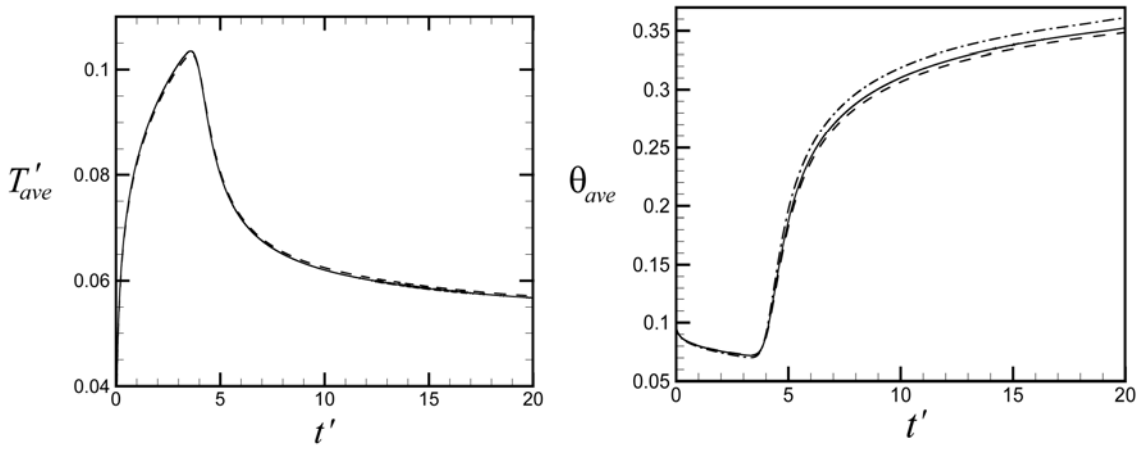

(a) (b)

Figure 2. Time variation of the average cable surface temperature and moisture content for the grid independence study, for grids A (dash-dot), B (solid), and C (dashed).

The sensitivity of the temperature field to the thermal convection term was examined by repeating the computation described above with grid B but with no thermal convection term. The prediction for the average dimensionless temperature on the cable surface is compared with the result with the thermal convection term in Figure 3. It is observed that the results are similar for the runs with and without convection during the initial part of the calculation as the cable temperature increases before the rain front penetrates to the cable location. At about $t' = 4$, the cable temperature abruptly begins decreasing, coinciding with the abrupt increase in moisture content observed in Figure 2b associated with arrival of the moisture front from the rainfall event at the cable location. Following this time, the predictions with and without the convection term in Figure 3 exhibit significant differences. The most noticeable of these differences is that the cable temperature prediction without convection rapidly asymptotes to a constant value following arrival of the moisture front, whereas the cable temperature prediction with convection exhibits a gradual decrease with time.

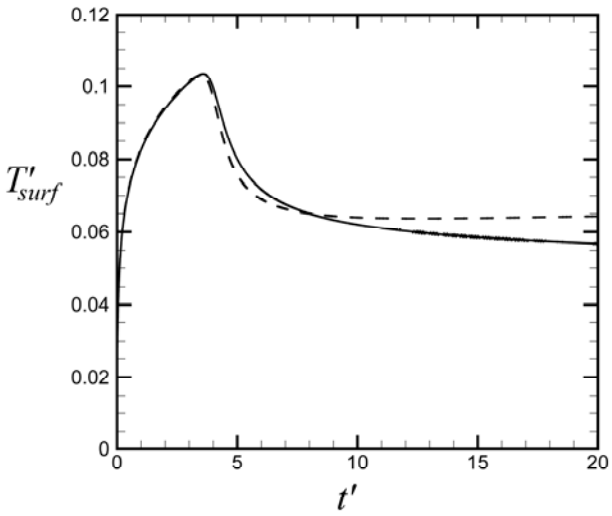

Figure 3. Comparison of predicted dimensionless average cable surface temperature for a case with the thermal convection term (solid line) and without the thermal convection term (dashed line) for the same run as shown in Figure 2.

3. Results and Discussion

Computational results are reported in this section for thermal and moisture fields around underground cables with periodic rainfall events. The rainfall intensity, duration, and period are all varied in such a way that the average rainfall is held constant, and the results are compared to computations with constant average rainfall in order to determine the transient effects caused by rainfall events.

Initialization

The computations are initialized using two sets of preliminary computations. The first preliminary computation is performed with the outer grid only for constant rainfall and with no cable present. Since this problem is essentially one-dimensional, the outer grid is reduced to 637 points in the *y*-direction and 11 points in the *x*-direction for the first preliminary computation. The constant rainfall rate is determined by dividing the average annual precipitation in different regions by the number of days in a year, and then non-dimensionalized to obtain $\overline{Q}'_{rain}$, where the overbar denotes average value. Computations were performed with $\overline{Q}'_{rain} = 0.005$, 0.01, 0.02, and 0.03, as well as the case with no rain ($\overline{Q}'_{rain} = 0$). The case with $\overline{Q}'_{rain} = 0.03$ corresponds to a precipitation of 95 cm/yr, which is typical of Chicago, whereas that with $\overline{Q}'_{rain} = 0.01$ corresponds to a precipitation of 32 cm/yr, which is typical of Los Angeles. For simplicity, rainfall is spread throughout the year and seasonal variations are ignored. Each computation is initialized using a uniform moisture content of $\theta_0 = 0.1$ and temperature set equal to the ambient value. The computations are continued until a steady-state condition is achieved in the value of moisture content to at least four significant figures. The case with no rain

did not achieve a steady-state value even after very long time, but instead decreased very slowly with time in a continuous manner. The steady-state moisture profiles for the four cases with non-zero values of $\overline{Q}'_{rain}$ are plotted as functions of the dimensionless depth $\xi \equiv -y/b$ in Figure 4. The line denoted by 'E' in this figure shows the moisture content profile for the case with no rain at a time approximately 10 years after the initial condition.

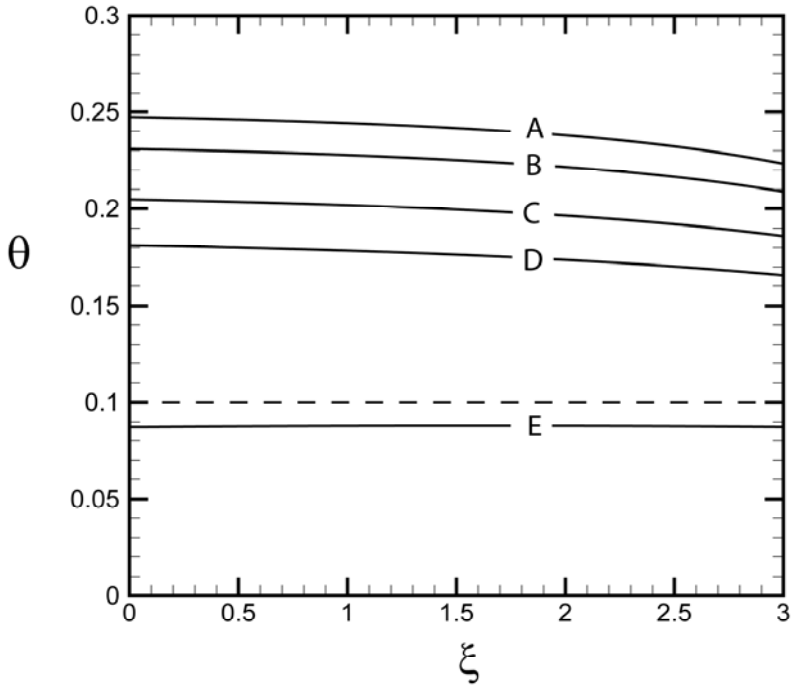

Figure 4. Steady-state moisture content profiles for cases with (A) $\overline{Q}'_{rain} = 0.03$, (B) 0.02, (C) 0.01, (D) 0.005, and (E) 0 as a function of dimensionless depth ξ. The initial moisture profile in the calculations is indicated by a dashed line. For the case with no rain, the moisture content moves downward very slowly in time and no steady-state profile is observed. The moisture profile shown in E is plotted at a time of approximately 10 years after the initial condition. The other cases have all converged to steady-state profiles within four significant figures in the moisture content.

The second preliminary computation reads in the equilibrium moisture content profile for the selected average rainfall rate, and then introduces the cable with a constant surface heat flux using both the outer and inner grids with the number of grid points set equal to the values stated for grid B in Table 3. In the second preliminary computation, the rainfall rate is held constant at the same average value as used for the first computation. The computations are continued until both the temperature and moisture content fields have achieved steady-state values. The time variation of the average temperature and moisture content on the cable surface are plotted in Figure 5 as functions of time for the four cases with non-zero rainfall shown in Figure 4, showing the approach of the results to a steady-state condition. In Figure 5a, the dimensionless temperature is shown on the left-hand *y*-axis and the corresponding change in dimensional temperature (in $^{\circ}C$) for the example problem with $\overline{q} = 500\ \mathrm{W/m^2}$, $b = 1\ \mathrm{m}$, and $\lambda_0 = 1.6\ \mathrm{W/mK}$ is shown on the right-hand *y*-axis.

Table 3. Number of points in different grids used in grid independence study.

Grid Identification	**Outer Grid**		**Inner Grid**	
	x	y	r	ϕ
A	651	451	37	63
B	921	637	53	89
C	1029	711	59	99

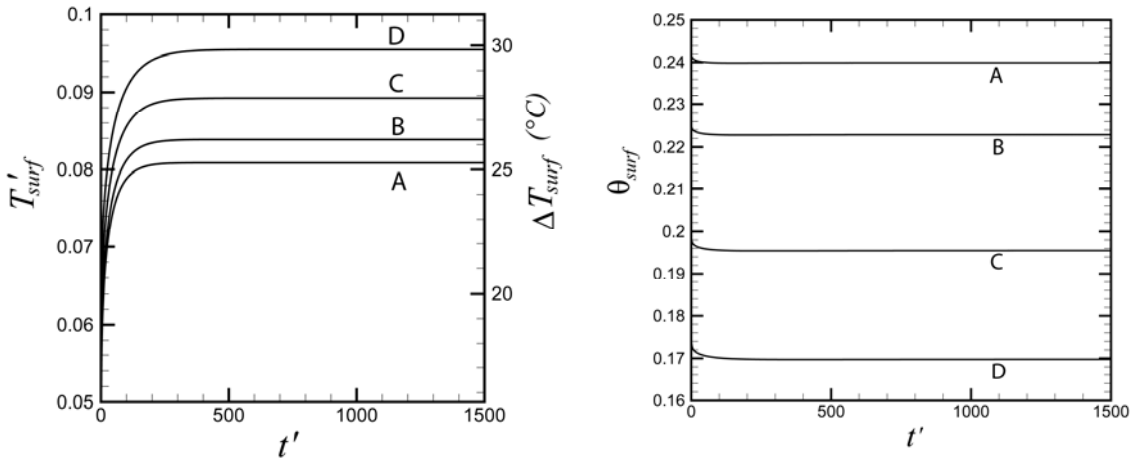

(a) (b)

Figure 5. Time variation of the average cable surface (a) temperature and (b) moisture content during the second preliminary computation for cases with (A) $\overline{Q}'_{rain} = 0.03$, (B) 0.02, (C) 0.01, and (D) 0.005. In (a), the dimensionless temperature is shown on the left-hand *y*-axis and the corresponding change in dimensional temperature for the example problem is shown on the right-hand *y*-axis. The figure shows the approach of the temperature and moisture content fields to a steady state condition.

The contours of the steady-state temperature and moisture content around the cable are plotted for the case with $\overline{Q}'_{rain} = 0.03$ in Figure 6. In this figure, the near-cable inner grid is superimposed on the outer grid so that the fields are accurately represented both near to and far away from the cable. Contours of the temperature and moisture content fields are observed in close-up images to vary smoothly and continuously across the two grids. Also, the value of temperature and moisture content is extracted on the vertical line $x = 0$, passing through the cable, and plotted in Figure 7 for the four different rainfall rates in their steady-state solutions. As expected, the temperature field exhibits a local maximum at the cable and decays away from the cable. From Figure 7, we observe that the temperature peak value does not differ significantly between the four different rainfall rates examined, although the temperature falls off more rapidly with

distance away from the cable for the higher rainfall rate case, as is consistent with the higher thermal conductivity caused by higher values of moisture content. The moisture content exhibits a local minimum near the cable for all four rainfall rates, which corresponds to a region in which the moisture content contour lines are locally raised upward as they pass over the cable. This effect also persists for some distance below the cable. The presence of rainfall causes the region of decreased moisture fraction (i.e., the 'dry' region) surrounding the cable to become asymmetric, with a sharper moisture gradient above the cable than below the cable.

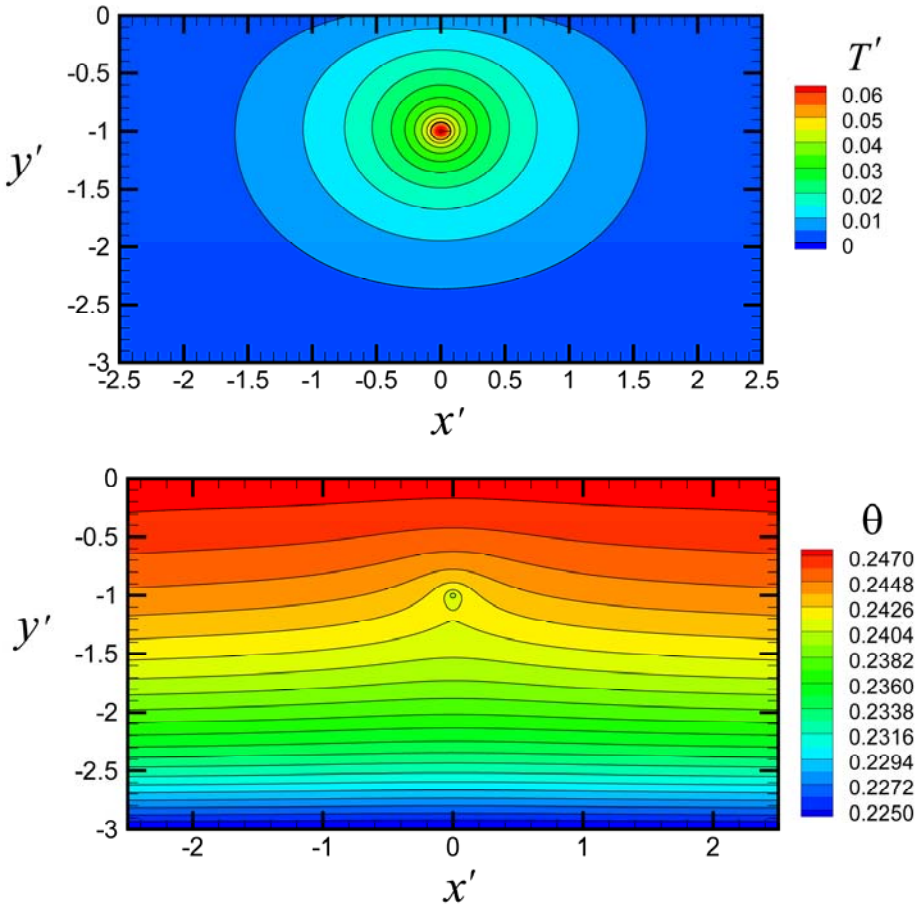

Figure 6. Steady-state (a) dimensionless temperature and (b) moisture content fields at the end of the second preliminary computation for the case with $\overline{Q}'_{rain} = 0.03$.

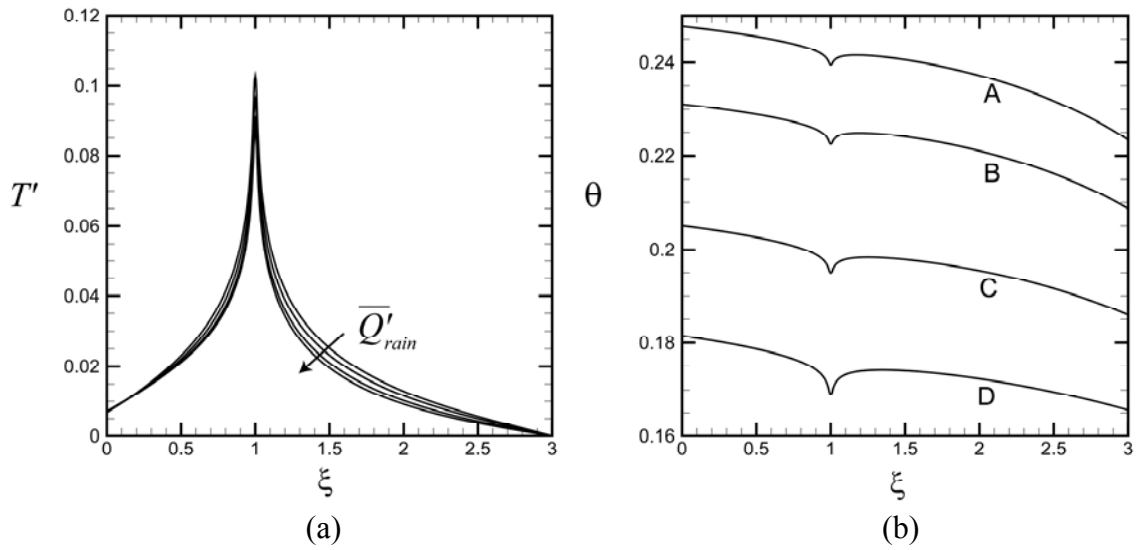

Figure 7. Variation of (a) temperature and (b) moisture content on the line $x' = 0$ as a function of dimensionless depth ξ for the same four values of $\overline{Q}'_{rain}$ shown in Figure 5.

Periodic Variation in Rainfall Intensity, Duration, and Frequency

The result of the second preliminary computation is used as an initial condition for a series of computations examining the effect of rainfall transients on cable thermal and moisture exposure. In each of these computations, the rainfall is assumed to occur periodically in time, with intensity, duration, and frequency that are consistent with the specified average rainfall rate in the preliminary computations. Each set of computations is compared with the result of the steady-state computation with constant rainfall rate. We focus specifically on two regions, one fairly moist (typical of Chicago, Illinois) and one fairly dry (typical of Los Angeles, California). The average dimensionless rainfall rates for these two regions are approximately $\overline{Q}'_{rain} \cong 0.03$ and 0.01, corresponding to 940 and 325 mm/yr, respectively. According to Sun et al. (2006), 67% of the precipitation occurs in 15 days in Los Angeles and in 30 days in Chicago, yielding a dimensionless frequency of $f' \equiv f\tau_L$ of 0.04 and 0.08, respectively. Rainfall intensity varies from about 2.5

mm/hr for a light rainfall to between 10-50 mm/hr for a heavy rainfall, with a characteristic value of 10 mm/hr for a moderate rainfall. When non-dimensionalized using $K_{\theta 0} = 10^{-6}$ m/s, the characteristic value of the instantaneous dimensionless rainfall intensity, Q'_{rain}, is approximately 2.5. Dividing the total annual precipitation by the characteristic rainfall intensity (10 mm/hr) times the number of rainy days gives a typical rainfall duration of about 2.5 hours, or $D_{rain} = 2.5/24 \cong 0.1$. Using these characteristic values, a listing of computational runs was formulated as shown in Table 4. The first runs D1 and M1 are based on the characteristic conditions, runs D2-D3 and M2-M3 vary intensity and duration with fixed frequency, runs D4-D5 and M4-M5 vary duration and frequency with fixed intensity, and runs D6-D7 and M6-M7 vary intensity and frequency with fixed duration.

Results are shown in Figures 8-10 for Run D1, characteristic of a dry climate (e.g., Los Angeles). The average cable surface temperature and moisture content are plotted in Figure 8 as functions of time. The computation is performed over a time interval of 600 days, during which 24 rainfall periods occur. Even though the computation is initialized at the steady-state condition for the same value of average rainfall rate as used in the D1 computation, it is observed that the temperature and moisture fields approach a periodic limit-cycle state in which the mean temperature and moisture content on the cable surface has very different values than in the steady-state condition. The approach of the system from the steady-state solution to a limit-cycle state is shown in Figure 9, which plots the dimensionless cable surface temperature as a function of the cable surface moisture content. In this limit-cycle condition, the mean cable surface dimensionless temperature decreases by about 0.008 and the mean moisture

content increases by about 0.04 compared to the steady-state solution. The oscillation amplitude of the dimensionless cable surface temperature in the limit-cycle state is $T'_{amp} \cong 0.0003$ and the amplitude of the moisture content on the cable surface is $\theta_{amp} \cong 0.0044$.

Table 4. Listing of rainfall conditions used for periodic rainfall computations in conditions typical of dry and moist climates. Rainfall is characterized by the dimensionless rainfall intensity $Q'_{rain} = Q_{rain} / K_{\theta 0}$, duration $D_{rain} = \tau_R / \tau_L$, and frequency $f' = f\tau_L$. The computational results are listed for the change in the mean values of dimensionless temperature and moisture content from the steady-state solutions, $\Delta\overline{T}'_{surf}$ and $\Delta\overline{\theta}_{surf}$, and the oscillation amplitude of the dimensionless temperature and moisture content in the periodic solution, T'_{amp} and θ_{amp}.

Dry Climate ($\overline{Q}'_{rain} = 0.01$)							
Rainfall Characteristics				Computational Results			
Run	Intensity	Duration	Freq.	$\Delta\overline{T}'_{surf}$	T'_{amp}	$\Delta\overline{\theta}_{surf}$	θ_{amp}
D1	2.5	0.10	0.04	- 0.0081	0.00031	0.040	0.0044
D2	1.0	0.25	0.04	- 0.0076	0.00029	0.037	0.0041
D3	5.0	0.05	0.04	- 0.0097	0.00039	0.040	0.0052
D4	2.5	0.20	0.02	- 0.0085	0.00093	0.042	0.0115
D5	2.5	0.05	0.08	- 0.0074	0.00009	0.037	0.0015
D6	5.0	0.10	0.02	- 0.0104	0.00130	0.045	0.0146
D7	1.25	0.10	0.08	- 0.0067	0.00008	0.033	0.0013
Moist Climate ($\overline{Q}'_{rain} = 0.03$)							
Rainfall Characteristics				Computational Results			
Run	Intensity	Duration	Freq.	$\Delta\overline{T}'_{surf}$	T'_{amp}	$\Delta\overline{\theta}_{surf}$	θ_{amp}
M1	2.5	0.15	0.08	- 0.0094	0.00038	0.050	0.0060
M2	1.0	0.375	0.08	- 0.0088	0.00036	0.047	0.0058
M3	5.0	0.075	0.08	- 0.0082	0.00043	0.044	0.0069
M4	2.5	0.30	0.04	- 0.0101	0.00111	0.056	0.0145
M5	2.5	0.075	0.16	-0.0077	0.00012	0.042	0.0020
M6	5.0	0.15	0.04	-0.0088	0.00127	0.048	0.0170
M7	1.25	0.15	0.16	-0.0073	0.00011	0.040	0.0021

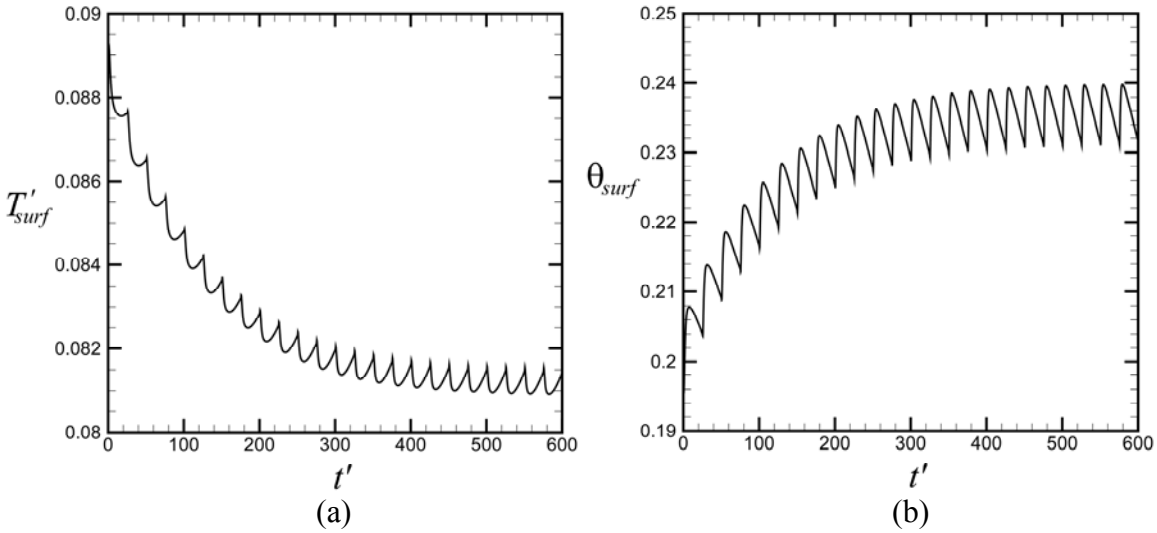

Figure 8. Oscillation of average dimensionless temperature and moisture content on the cable surface as functions of dimensionless time with constant cable heat flux, for Run D1. The oscillations observed in the plots are due to periodic rain events.

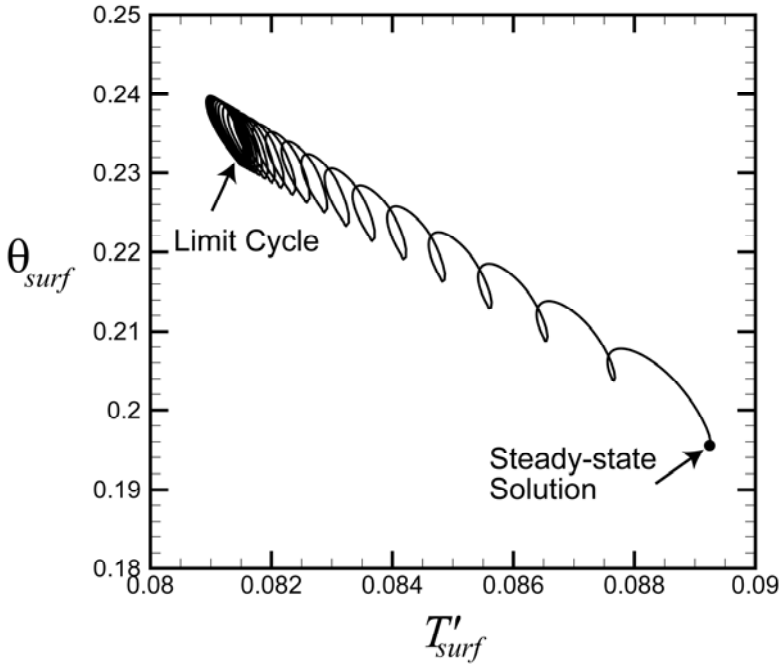

Figure 9. Plot of dimensionless cable surface temperature as a function of cable surface moisture content for Run D1, showing the approach of the system to a limit-cycle behavior at long time.

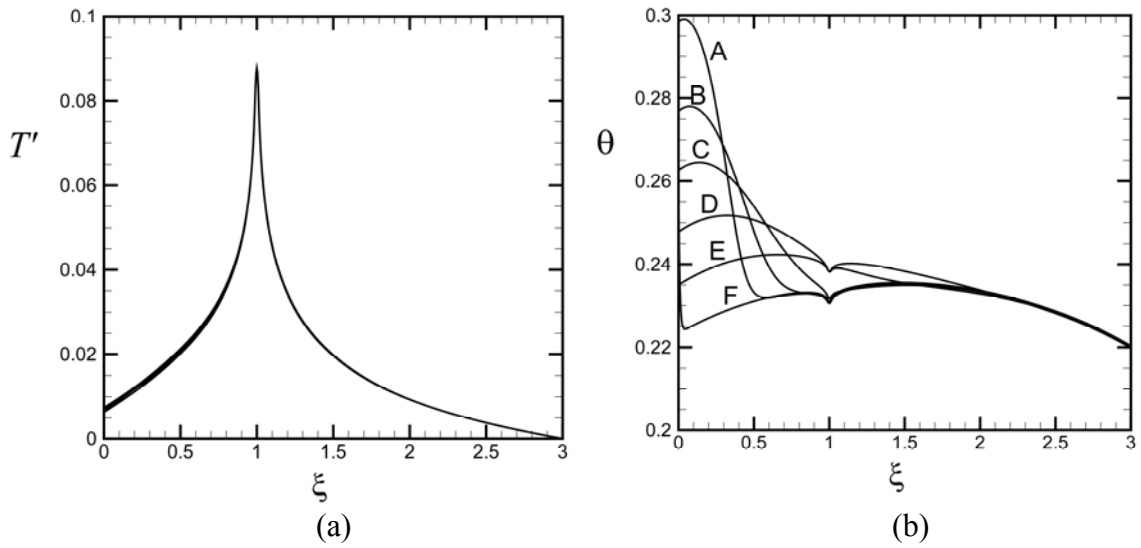

Figure 10. Variation of (a) dimensionless temperature and (b) moisture content on the line $x' = 0$ as a function of the dimensionless depth ξ for Run D1 at times (A) $t' = 575.2$, (B) 575.4, (C) 575.8, (D) 577.2, (E) 583.6, and (F) 575 and 600. The same six lines are plotted in (a), but the curves nearly overlap.

Plots showing the variation in temperature and moisture content profiles during a periodic rainfall event are given in Figure 10, for a time period $t' = [575,600]$ at which the system has achieved a periodic state. The profiles are extracted along the line $x' = 0$, which passes through the cable at depth $\xi = 1$. The largest moisture content variation occurs near the ground surface ($\xi = 0$) during the first part of the period, during and immediately after the rainfall event. The curves in this figure are plotted at times that are chosen so as to capture this moisture spike, and hence are preferentially timed for the beginning part of the rain period. Profiles are plotted at the same times in Figures 10a and 10b, but the temperature change due to moisture content variation is sufficiently small compared to the steady-state temperature values that the curves nearly lie on top of each other in Figure 10a. In Figure 10b, the rainfall is observed to cause a spike in moisture content near the ground surface $\xi = 0$. This rainfall spike rapidly propagates into the soil,

and it diffuses and reduces in magnitude as it does so. Several different effects occur to influence the moisture content profiles, including downward gravitational drainage, upward pulling from the capillary force, diffusive spreading, and repulsion of moisture from the cable due to the temperature gradient around the cable. The combination of these influences causes the large fluctuation amplitude of the moisture content at the ground level ($\xi = 0$), which measures approximately 0.04, to decrease by nearly an order of magnitude at the level of the cable ($\xi = 1$). The moisture content fluctuation continues to decrease such that there is almost no observable change with time for depths $\xi < 2$. Following the rainfall event, the moisture content profile gradually returns to a curve with local maximum at approximately $\xi = 1.6$. This curve differs significantly in structure from the moisture content profile given in Figure 7b for the steady-state case.

Contour plots of the moisture content field are shown in Figure 11 for one day following a rainfall event in Run D1. The figure is plotted starting at time $t' = 575$, by which point the system has achieved a periodic state. The initial plot (Figure 11a) is for an instance just before the rain begins. The structure of the moisture field has a region of high moisture content centered at about $\xi = 1.3$, with low moisture near both the bottom and the top of the computational domain. This high moisture band is the remnant of previous rainfalls, which are pulled downward by gravity and upward by capillary action. The region surrounding the cable is observed to be drier than surrounding regions at the same level, as evidenced by a downward deflection of the moisture contour lines. This structure differs significantly from that shown in Figure 6b for the steady-state simulation. At time $t' = 575.2$ (Figure 11b), the rain event has recently ended and a region with high moisture content is observed at the top of the figure. This region of high

moisture content propagates downward with time in Figures 11c-f, eventually overtaking the dry region around the cable. Over longer time, the high-moisture region from the previous rainfall will move downward and merge into the high-moisture region located just below the cable, so that by the end of the period at $t' = 600$, the moisture field looks the same as shown in Figure 11a.

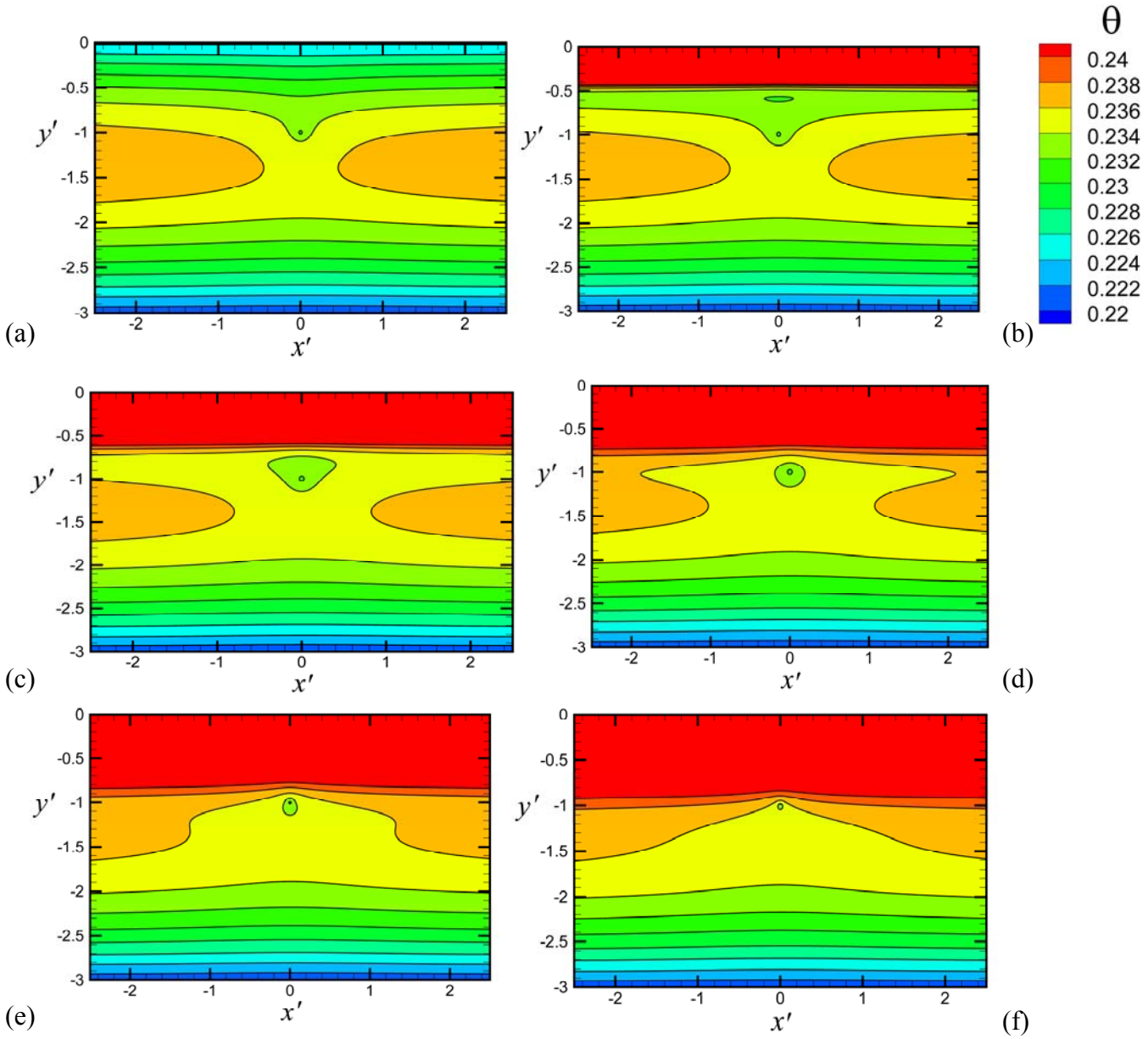

Figure 11. Contour plot of the moisture content for a time interval of one day following a rain storm, for Run D1. The plots are made at dimensionless times (a) $t' = 575$, (b) 575.2, (c) 575.4, (d) 575.6, (e) 575.8, and (f) 576.

Results are presented in Figures 12 and 13 for Run M1, characteristic of a moderately moisture climate (e.g, Chicago). The trends in the data are qualitatively the same as was observed under drier conditions in Figures 8 and 10. The cable surface temperature and moisture content transition from the steady-state solution to approach a limit-cycle state. The mean dimensionless cable surface temperature decreases by about 0.0094 and the mean cable surface moisture content increases by about 0.050 in this limit-cycle state compared to the values in the steady-state solution. The fluctuations in dimensionless surface temperature and moisture content during each rainfall cycle occur with amplitude $T'_{amp} \cong 0.0004$ and $\theta_{amp} \cong 0.006$, which are slightly larger than the values observed for Run D1. The temperature profile in Figure 13a is not significantly affected by the moisture variation, but the moisture profile in Figure 13b exhibits a large spike near the upper surface during and immediately after the rainfall event, with the moisture content increasing by approximately 0.1 at $\xi = 0$ during each rainfall cycle. As was the case with Run D1, the fluctuation in moisture content decays rapidly with depth, decreasing by about an order of magnitude by the level of the cable. The moisture content is observed to settle in the later part of each period to the same hump-type profile as noted in Figure 10b for Run D1, for which the moisture content is a maximum at an intermediate depth.

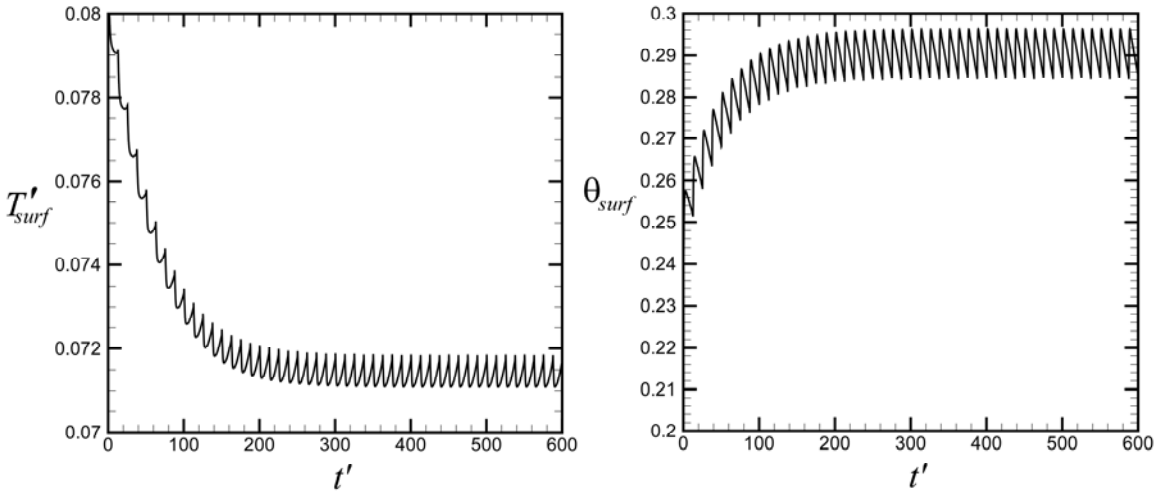

(a) (b)

Figure 12. Oscillation of average dimensionless temperature and moisture content on the cable surface as functions of dimensionless time with constant cable heat flux, for Run M1. The oscillations observed in the plots are due to periodic rain events.

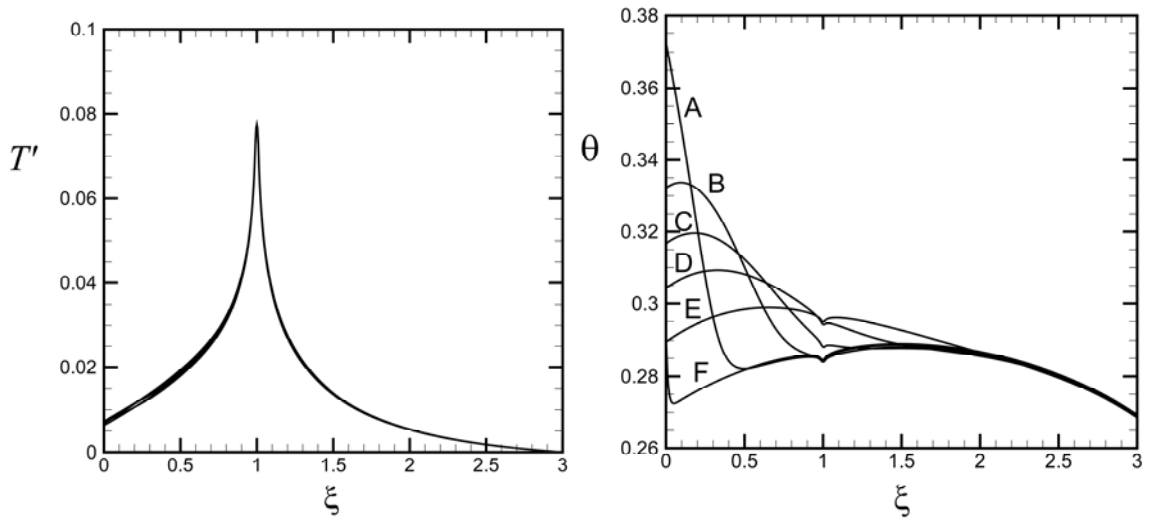

(a) (b)

Figure 13. Variation of (a) dimensionless temperature and (b) moisture content on the line $x' = 0$ as a function of the dimensionless depth ξ for Run M1 at times (A) $t' = 587.6$, (B) 587.8, (C) 588.0, (D) 588.4, and (E) 590.0, and (F) 587.5 and 600. The same six lines are plotted in (a), but they nearly overlap.

The system response for Runs D2-D7 and M2-M7 were qualitatively similar to that described above for Runs D1 and M1. In all cases with periodic rainfall, the cable surface temperature and moisture content approach a periodic limit-cycle condition in which the mean cable surface temperature decreases and the mean cable surface moisture content increases compared to the steady-state solutions. A listing of the change in dimensionless cable surface temperature and moisture content and the amplitude of oscillation of these values in the limit-cycle state is given in Table 4 for Runs D1-D7 and M1-M7. The results in this table exhibit a strong dependence of the oscillation amplitude on the rain frequency, but a weaker dependence on rainfall intensity and duration (provided the total rainfall amount is fixed).

Figure 14 plots the computed oscillation amplitude for the dimensionless cable surface temperature and the cable moisture content as functions of dimensionless frequency f' for all of the conditions examined. The oscillation amplitude values for the moist conditions (Runs M1-M7) are substantially greater than for the dry conditions (Runs D1-D7). The amplitudes for the cable surface temperature and moisture content decrease as the rainfall frequency increases. Since the total annual rainfall amount for the dry and moist conditions is fixed, higher frequency cases correspond to conditions with frequent rainfall events containing small amounts of precipitation, whereas low frequency cases correspond to conditions with infrequent rainfall events that contain large amounts of precipitation. It is noted that the oscillation amplitude is rather small for both the cable surface temperature and the moisture content. For instance, for the example problem with burial depth $b = 1\,\text{m}$ and average cable heat flux $\overline{q}$ = 500 W/m^2, the largest oscillation amplitude values for the cable surface temperature and moisture content in the

computations conducted were $0.4°C$ and 0.017, respectively. By comparison, the temperature field obtained by Marshall et al. (2013) for the same example case oscillated due to the daily power load variation with amplitude of $3.9°C$, or an order of magnitude larger than the rain-related oscillation amplitude.

Plots are shown in Figure 15 for the difference between the dimensionless cable surface temperature and the cable surface moisture content in the periodic limit-cycle condition and the initial values for the steady-state case, denoted by $\Delta T'_{mean}$ and $\Delta\theta_{mean}$. The dimensionless cable surface temperature decreases with periodic rainfall by an amount between 0.006 and 0.011, where the magnitude of the temperature change decreases with increase in the rainfall frequency. The cable surface moisture content increases with periodic rainfall by an amount ranging between 0.033 and 0.056, where the change in moisture content also decreases with increase in rainfall frequency. Again using our example problem with $b = 1\,\text{m}$ and $\overline{q}$ = 500 W/m^2, the change in mean cable surface temperature under the periodic rainfall condition corresponds to a decrease of $2.0 - 3.5°C$.

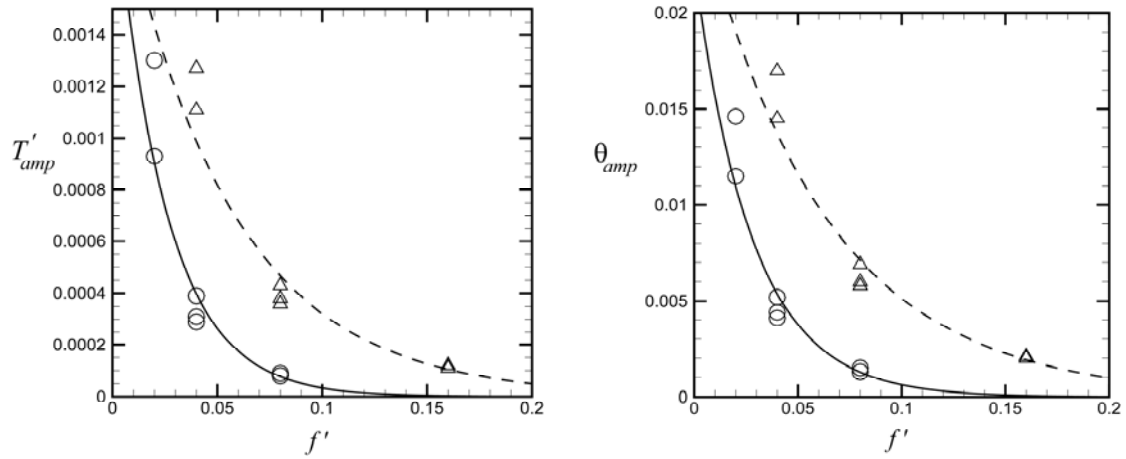

(a) (b)

Figure 14. Amplitude of average cable surface (a) dimensionless temperature and (b) moisture content fluctuations with periodic rain events as functions of dimensionless frequency. Results are for the moist condition (triangles, dashed line) and the dry condition (circles, solid line) listed in Table 4. The curves are exponential fits to the data.

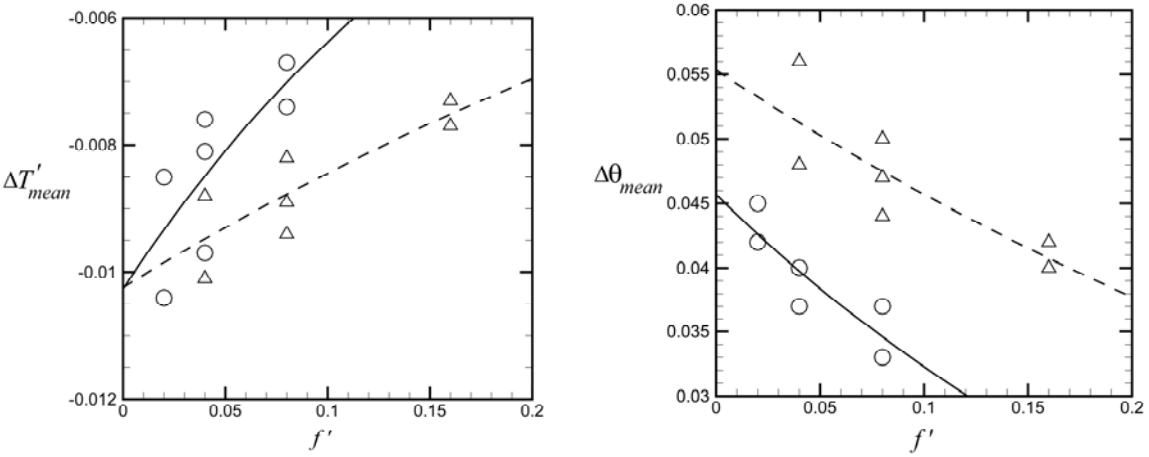

(a) (b)

Figure 15. Change in mean values of the average cable surface (a) dimensionless temperature and (b) moisture content with periodic rain events as functions of dimensionless frequency. Results are for the moist condition (triangles, dashed line) and the dry condition (circles, solid line) listed in Table 4. The curves are exponential fits to the data.

4. Conclusions

A study of the effect of periodic rainfall events on the surface temperature and moisture exposure of a buried electric cable was conducted using numerical simulations. Cases with different rainfall intensity, duration, and frequency were compared to a steady-state case with the same annual precipitation amount. Computations were conduced for two values of the annual precipitation, one typical of a relatively moist climate and one typical of a dry climate. In the steady-state condition, the computations indicate formation of a relatively dry region surrounding the cable in which the moisture content decreases by about 2-5% compared to the value that it would have had without the cable present. Under periodic rainfall conditions, the cable surface temperature and moisture content transition to a limit-cycle behavior with values that oscillate periodically in time with the rainfall frequency. Of particular interest is the observation that the mean values of the cable surface temperature and moisture content in this limit-cycle condition are significantly different from the steady-state values, with the mean cable surface temperature decreasing and the moisture content increasing in value under the limit-cycle condition relative to the steady-state condition. Both the oscillation amplitudes and the change in mean values relative to the steady-state condition are observed to depend primarily on the rainfall frequency and on the annual precipitation amount, such that the absolute values of these quantities decrease as the rainfall frequency or the annual precipitation amount increase. While the computed values of the oscillation amplitude of the cable surface temperature are rather small, measuring $0.4°C$ or less in the current computations, the change in the mean cable surface temperature between the steady-state and limit-cycle conditions is found to be large, measuring as high as $3.5°C$ in the current

computations. Similarly, the largest computed value of the oscillation amplitude of the moisture content (0.017) is small compared to the largest computed value of the change in mean cable surface moisture content between the limit-cycle and steady-state conditions (0.056).

The results of the current study have shown that periodic rainfall conditions result in fundamentally different moisture and temperature fields around an underground cable compared to what would be observed under rainfall steady-state conditions. Not only do the moisture content and temperature values oscillate periodically in time when exposed to periodic rainfall events, but the time-averaged values of the moisture content and temperature also change significantly in this periodic case compared to their steady-state values. The change in the mean values causes decreased values of the cable surface temperature, but increased values of the cable surface moisture content. As a consequence, steady-state computations over-estimate the temperature-related degradation of the cable insulation but under-estimate the moisture-related insulation degradation.

Acknowledgements

The authors appreciate discussions with George Pinder on the groundwater transport modeling. This work was sponsored by the U.S. Dept. of Transportation, through the University of Vermont Transportation Research Center (Grant TRC039).

References

G.J. Anders, *Rating of Electric Power Cables. Ampacity Computations for Transmission, Distribution, and Industrial Applications*, IEEE Press, New York, 1997.

G. J. Anders, M. A. El-Kady, Transient ratings of buried power cables. Part 1. Historical perspective and mathematical model, *IEEE Trans Power Delivery* **7**(4) (1992) 1724-1734.

G.J. Anders, H. S. Radhakrishna, Computation of temperature field and moisture content in the vicinity of current-carrying underground power cables, *IEEE Trans* **135C** (1988) 51-61.

W.Z. Black, S. I. Park, Emergency ampacities of direct buried three phase underground cable systems, *IEEE Trans Power Apparatus Systems* **102**(7) (1983) 2124-2132.

K. Clement-Nyns, E. Haesen, J. Driesen, The impact of charging plug-in hybrid electric vehicles on a residential distribution grid, *IEEE Trans. Power Systems* **25**(1) (2010) 371-380.

L. P. Fernández, T. G. San Román, R. Cossent, C. M. Domingo, P. Frías, Assessment of the impact of plug-in electric vehicles on distribution networks, *IEEE Trans. Power Systems* **26**(1) (2011) 206-213.

N. Flatabo, Transient heat conduction problems in power cables solved by finite element method, *IEEE Trans Power Apparatus Systems* **92**(1) (1973) 56-63.

D. S. Freitas, A. T. Prata, A. J. de Lima, Thermal performance of underground power cables with constant and cyclic currents in presence of moisture migration in the surrounding soil, *IEEE Trans. Power Delivery* **11**(3) (1996) 1159-1170.

C. Garrido, A. F. Otero, J. Cidrás, Theoretical model to calculate steady state and transient ampacity and temperature in buried cables, *IEEE Trans Power Del* **18**(3) (2003) 667-678.

G. Gela, J. J. Dai, Calculation of thermal fields of underground cables using the boundary element method, *IEEE Trans Power Delivery* **3**(4) (1988) 1341-1347.

M.A. Hanna, A.Y. Chikhani, M. M. A. Salama, Thermal analysis of power cables in multi-layered soil. Part 1. Theoretical model, *IEEE Trans Power Delivery* **8**(3) (1993) 761-771.

I.N. Hamdhan, B.G. Clarke, Determination of thermal conductivity of coarse and fine sand soils. Proceedings World Geothermal Congress, Bali, Indonesia, 25-29 April (2010).

P. Hyvönen, Prediction of insulation degradation of distribution power cables based on chemical analysis and electrical measurements, Ph.D. dissertation, Helsinki University of Technology, 2008.

M.A. Kellow, A numerical procedure for the calculation of the temperature rise and ampacity of underground cables, *IEEE Trans Power Apparatus Sys* **100**(7) (1981) 3322-3330.

N. Kovač, I. Sarajčev, D. Poljak, Nonlinear-coupled electric-thermal modeling of underground cable systems, *IEEE Trans Power Delivery* **21**(1) (2006) 4-14.

M. Liang, An assessment of conductor temperature rises of cables caused by a sudden application of short pulse in a daily cycle load, *IEEE Trans Power Del* **14**(2) (1999) 307-313.

J.S. Marshall, P.D. Hines, J.D. Zhang, F. Minervini, S. Rinjitham, Modeling the impact of electric vehicle charging on heat transfer around underground cables, *Electric Power Systems Research* **97** (2013) 76-83.

G. Mazzanti, Analysis of the combined effects of load cycling, thermal transients and electrothermal stress of life expectancy of high-voltage AC cables, *IEEE Trans. Power Delivery* **22**(4) (2007) 2000-2009.

G. Mazzanti, The combination of electro-thermal stress, load cycling and thermal transients and its effects on the life of high voltage ac cables, *IEEE Trans Dielectrics Electrical Insulation* **16**(4) (2009) 1168-1179.

G. C. Montanari, G. Mazzanti, L. Simoni, Progress in electrothermal life modeling of electrical insulation over the last decades, *IEEE Trans Dielectrics Electrical Insulation* **9**(5) (2002) 730-745.

R.E.S. Moya, A.T. Prata, J.A.B. Cunha Neto, Experimental analysis of unsteady heat and moisture transfer around a heated cylinder buried into a porous medium. *International Journal of Heat and Mass Transfer* **42**, 2187-2198 (1999).

J. Nahman, M. Tanaskovic, Calculation of the ampacity of medium voltage self-supporting cable bunch, *Electric Power Systems Research* **93** (2012) 106-112.

J. H. Neher, M. H. McGrath, The calculation of the temperature rise and load capability of cable systems, *AIEE Trans*, Part 3, **752-763** (1957) 752-763.

J. H. Neher, The transient temperature rise of buried cable systems, *IEEE Trans. Power Apparatus Systems* **83**(2) (1964) 102-114.

J.R. Philip, D.A. de Vries, Moisture movement in porous materials under temperature gradients. *Transactions of the American Geophysical Union* **38**, 222-232 (1957).

P. Rezaei, J. Frolik, P. Hines. Packetized plug-in electric vehicle charge management. *IEEE Transactions on Smart Grid* (in press, 2014).

Y. Sun, S. Solomon, A. Dai, and R.W. Portman, How Often Does It Rain? *Journal of Climate* **19** (2006) 916-934.

E. Tarasiewicz, E. Kuffel, and S. Grybowsji, Calculation of temperature distributions within cable trench backfill and the surrounding soil, *IEEE Trans. Power Apparatus Systems* **104**(8) (1985) 1973-1978.

L. R. Vollaro, J. Fontana, A. Vallati, Thermal analysis of underground electric power cables buried in non-homogeneous soils, *Applied Thermal Engineering* **31** (2011) 772-778.

R. Webster, Can the electricity distribution network cope with an influx of electric vehicles?, *J. Power Sources* **80**(1–2) (1999) 217–225.

Figure Captions

Figure 1. Schematic diagram of the computational flow domain and the inner (polar) and outer (Cartesian) grids, where the cable is identified as a black circle at the center of the inner grid, which is submerged a depth *b* below the ground. The boundaries of the outer grid are identified by circled numbers.

Figure 2. Time variation of the average cable surface temperature and moisture content for the grid independence study, for grids A (dash-dot), B (solid), and C (dashed).

Figure 3. Comparison of predicted dimensionless average cable surface temperature for a case with the thermal convection term (solid line) and without the thermal convection term (dashed line) for the same run as shown in Figure 2.

Figure 4. Steady-state moisture content profiles for cases with (A) $\overline{Q}'_{rain} = 0.03$, (B) 0.02, (C) 0.01, (D) 0.005, and (E) 0 as a function of dimensionless depth ξ. The initial moisture profile in the calculations is indicated by a dashed line. For the case with no rain, the moisture content moves downward very slowly in time and no steady-state profile is observed. The moisture profile shown in E is plotted at a time of approximately 10 years after the initial condition. The other cases have all converged to steady-state profiles within four significant figures in the moisture content.

Figure 5. Time variation of the average cable surface (a) temperature and (b) moisture content during the second preliminary computation for cases with (A) $\overline{Q}'_{rain} = 0.03$, (B) 0.02, (C) 0.01, and (D) 0.005. In (a), the dimensionless temperature is shown on the left-hand *y*-axis and the corresponding change in dimensional temperature for the example problem is shown on the right-hand *y*-axis. The figure shows the approach of the temperature and moisture content fields to a steady state condition.

Figure 6. Steady-state (a) dimensionless temperature and (b) moisture content fields at the end of the second preliminary computation for the case with $\overline{Q}'_{rain} = 0.03$.

Figure 7. Variation of (a) temperature and (b) moisture content on the line $x' = 0$ as a function of dimensionless depth ξ for the same four values of $\overline{Q}'_{rain}$ shown in Figure 5.

Figure 8. Oscillation of average dimensionless temperature and moisture content on the cable surface as functions of dimensionless time with constant cable heat flux, for Run D1. The oscillations observed in the plots are due to periodic rain events.

Figure 9. Plot of dimensionless cable surface temperature as a function of cable surface moisture content for Run D1, showing the approach of the system to a limit-cycle behavior at long time.

Figure 10. Variation of (a) dimensionless temperature and (b) moisture content on the line $x' = 0$ as a function of the dimensionless depth ξ for Run D1 at times (A) $t' = 575.2$,

(B) 575.4, (C) 575.8, (D) 577.2, (E) 583.6, and (F) 575 and 600. The same six lines are plotted in (a), but the curves nearly overlap.

Figure 11. Contour plot of the moisture content for a time interval of one day following a rain storm, for Run D1. The plots are made at dimensionless times (a) $t' = 575$, (b) 575.2, (c) 575.4, (d) 575.6, (e) 575.8, and (f) 576.

Figure 12. Oscillation of average dimensionless temperature and moisture content on the cable surface as functions of dimensionless time with constant cable heat flux, for Run M1. The oscillations observed in the plots are due to periodic rain events.

Figure 13. Variation of (a) dimensionless temperature and (b) moisture content on the line $x' = 0$ as a function of the dimensionless depth ξ for Run M1 at times (A) $t' = 587.6$, (B) 587.8, (C) 588.0, (D) 588.4, and (E) 590.0, and (F) 587.5 and 600. The same six lines are plotted in (a), but they nearly overlap.

Figure 14. Amplitude of average cable surface (a) dimensionless temperature and (b) moisture content fluctuations with periodic rain events as functions of dimensionless frequency. Results are for the moist condition (triangles, dashed line) and the dry condition (circles, solid line) listed in Table 4. The curves are exponential fits to the data.

Figure 15. Change in mean values of the average cable surface (a) dimensionless temperature and (b) moisture content with periodic rain events as functions of dimensionless frequency. Results are for the moist condition (triangles, dashed line) and the dry condition (circles, solid line) listed in Table 4. The curves are exponential fits to the data.